Contents

Chapter 1

Complex Light Beams

Enrique J. Galvez

Department of Physics and Astronomy, Colgate University

1.1 Introduction

Optical beams of light derived from lasers have been useful for many applications for a long time. The invention of lasers has led to our ability to control very precisely many parameters of the light, such as wavelength and time. In many cases the spatial mode and polarization of the light has remained constant. However, most recently, the technology has evolved to allow us greater control over the light, enabling us to control the phase, amplitude and polarization within a light beam. Complex light refers broadly to beams of light where one or more parameters are changed within the beam of light. In particular, spatial modes have received much attention, generated either directly from lasers or by manipulation of the wavefront via diffractive optical elements. These studies have led us to Laguerre-Gauss beams, Bessel beams and Airy beams. The control of their depth of focus and width have found application in high-resolution confocal and multiphoton microscopes at near or below the diffraction limit.

In this chapter article I delve into complex light by treating the most important beams of light that are useful for research in many areas of science and technology. It includes a description of the functional forms of the modes and their parameters, which lead to better resolution and deeper penetration into matter. I will first cover the fundamentals of Gaussian beams, which are naturally generated by a laser, and which constitute the workhorse of laser-based research on multiphoton and confocal microscopes, and in manipulation of matter via optical forces. I will then continue with

interesting optical realizations that carry a new range of physical phenomena, such as optical vortices and orbital angular momentum in the case of Laguerre-Gauss beams, diffraction-less propagation and self-reconstructing beams in the case of Bessel and Airy beams, or space-variant polarization and singularities in polarization in the case of vector and Poincaré beams. The different sections also discuss and cite the various methods for producing these beams. The hope is that they will stimulate new research in imaging, manipulation, and new areas where complex light has yet to make an impact, leading to the discovery of new phenomena and applications.

1.2 Gaussian beams

In this section we discuss optical beams that are described by a Gaussian intensity profile. This is the case of laser beams. Thus it is important to begin with a discussion of the fundamental Gaussian beam and its properties. We then follow with sections describing important high-order Gaussian beams, which are also beams that can be derived from the fundamental one.

1.2.1 Fundamental Gaussian beams

We begin by deriving the equation of the fundamental Gaussian beam. This treatment is also covered in standard textbooks on lasers [45, 40]. In classical electromagnetism, light is represented by an electromagnetic wave, with electric and magnetic fields that obey Maxwell's equations. Since the electric and magnetic fields are related to each other, it is usual to express light in terms of one of them: the electric field

$$\overrightarrow{E} = E_0 \Psi \hat{e}, \tag{1.1}$$

where E_0 is the scalar magnitude of the field of the beam, Ψ is a normalized wave function, and $\hat{e}$ is a unit vector. The scalar part of the field must satisfy the wave equation

$$\nabla^2 \Psi - \frac{1}{c^2} \frac{\partial^2 \Psi}{\partial t^2} = 0, \tag{1.2}$$

where

$$\nabla^2 = \frac{\partial}{\partial x^2} + \frac{\partial}{\partial y^2} + \frac{\partial}{\partial z^2}$$

is the Laplacian and c is the speed of the light. For a harmonic wave, we can introduce a trial solution that separates out the time dependence:

$$\Psi(x, y, x, t) = U(x, y, z)e^{-i\omega t}, \tag{1.3}$$

where U depends only on the spatial coordinates. Then by replacing Eq 1.3 into Eq. 1.2 we arrive at the Helmholtz equation:

$$\nabla^2 U + k^2 U = 0, \tag{1.4}$$

where $k = \omega/c$. We will be restricting ourselves to optical beams that are likely produced by lasers. These are collimated beams that have a finite transverse extent, and travel mainly in one dimension, say along the positive z axis of a Cartesian coordinate system. Thus we can require a solution to be similar to a plane wave, with a term $\exp(ikz)$. Therefore we propose that the solution has to be of the form

$$U(x, y, z) = U_0(x, y, z)e^{ikz}. \tag{1.5}$$

Replacing Eq. 1.5 into Eq. 1.4 and simplifying we get

$$\frac{\partial^2 U_0}{\partial x^2} + \frac{\partial^2 U_0}{\partial y^2} + \frac{\partial^2 U_0}{\partial z^2} + 2ik\frac{\partial U_0}{\partial z} = 0. \tag{1.6}$$

A beam is a wave of finite transverse extent, so diffraction causes the beam to spread as the light travels. To account for this diffraction we allow U_0 to depend on z. We can picture this the following way: the intensity of the light for fixed values of the transverse coordinates, x and y, is going to decrease as z increases. Thus we can say that U_0 changes slowly with z, and thus neglect the term $\partial^2 U_0/\partial z^2$ compared to the other ones and remove it from Eq. 1.6. The resulting equation is

$$\frac{\partial^2 U_0}{\partial x^2} + \frac{\partial^2 U_0}{\partial y^2} + 2ik\frac{\partial U_0}{\partial z} = 0. \tag{1.7}$$

It is called the paraxial wave equation.

We proceed to find U_0 by requiring that it have the form

$$U_0(x, y, z) = Ae^{\frac{ik(x^2+y^2)}{2q(z)}}e^{ip(z)}. \tag{1.8}$$

Replacing Eq. 1.8 into Eq. 1.7 we get separate equations for $q(z)$ and $p(z)$. The solution for $q(z)$ is

$$q(z) = z - iz_R, \tag{1.9}$$

where z_R is a constant known as the Rayleigh range. A more appropriate way to write this equation is

$$\frac{1}{q(z)} = \frac{1}{z + \frac{z_R^2}{z}} + \frac{i}{\frac{z^2}{z_R} + z_R}. \tag{1.10}$$

The solution for $p(z)$ is

$$e^{ip(z)} = \frac{w_0}{w}e^{-i\varphi(z)}, \tag{1.11}$$

Inserting Eqs. 1.10 and 1.11 into Eq. 1.8 yield

$$U_0(x, y, z) = A\frac{w_0}{w}e^{-\frac{x^2+y^2}{w^2}}e^{\frac{ik(x^2+y^2)}{2R}}e^{-i\varphi}, \tag{1.12}$$

where the beam spot of the beam w now depends on z:

$$w = w_0\sqrt{1 + \frac{z^2}{z_R^2}}, \tag{1.13}$$

4 | Complex Light Beams

and where the constant w_0 is called the beam waist. The Rayleigh range z_R is related to the waist by:

$$z_R = \frac{\pi w_0^2}{\lambda}. \qquad (1.14)$$

The above relation is the traditional and useful way to relate z_R and w_0, but a more intuitive relation is

$$\frac{z_R}{w_0} = \pi \frac{w_0}{\lambda}, \qquad (1.15)$$

relating the ratio of z_R and w_0 to the ratio of w_0 and λ. A new term that appears in the solution, R, is the radius of curvature of the wavefront, which also depends on z:

$$R = z + \frac{z_R^2}{z} \qquad (1.16)$$

Equation 1.12 also has a new phase φ, given by

$$\varphi = \tan^{-1}(z/z_R), \qquad (1.17)$$

and known as the Gouy phase.

Rewriting the solution to the wave function, we get

$$\Psi(x, y, z, t) = A \frac{w_0}{w} e^{-\frac{x^2+y^2}{w^2}} e^{i(kz-\omega t)} e^{\frac{ik(x^2+y^2)}{2R}} e^{-i\varphi} \qquad (1.18)$$

The first three terms specify the amplitude of the wave, and the next three terms contain the phase of the wave embedded in the exponential terms. It is important to understand the meaning of these terms, as they describe the properties of the beam. Below we analyze the most important features of them in detail.

1.2.1.1 The beam spot w

The function w of Eq. 1.13 represents the half width of the beam, also known as the beam spot. Figure 1.1. shows a graph of w as a function of z. When $z = 0$ the beam spot is w_0, also known as the waist, and is the smallest value that $w(z)$ can have under this description. In the positive and negative z directions w increases. Thus, the point $z = 0$ is either some type of starting point. Indeed, the central point of most lasers is a waist. Once the light comes out of a laser, its width w increases due to diffraction, which is accounted by the solution. Figure 1.1. also describes the width of a beam when it is focused by a lens. Below we will discuss how to control the size of the waist when we focus a beam of light. When $z = z_R$ the beam spot is $w = \sqrt{2}w_0$. This point is an important parameter in the propagation of the light: it marks the transition from the beam being nearly constant to one that increases linearly with z.

When we focus a beam of light with a converging lens, and think of the light as a set of parallel rays, we imagine those lines to cross exactly at the focal point. However, when $|z| < z_R$ the ray description of the propagation of the light breaks down, and the wave aspect sets in. When $z \gg z_R$ the waist becomes linearly dependent on the distance from the waist: $w \simeq (w_0/z_R)z$.
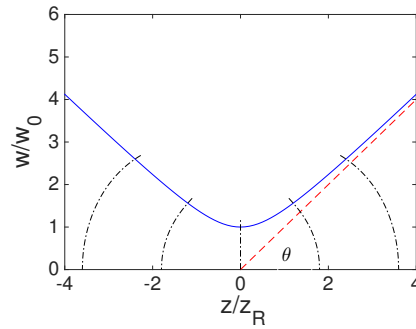
Figure 1.1.   Graph of the beam spot of the beam (solid blue) and wave-fronts (black, dash-dot). The red dashed line corresponds to the graph of $w = \theta z$ (see text).

This asymptote is shown by the red dashed line in Fig. 1.1. Because in this regime the beam spot expands nearly linearly, we can express it as

$$w = \theta z, \tag{1.19}$$

where θ is called the divergence angle of the beam, which, using Eq. 1.14, can be written as

$$\theta = \frac{\lambda}{\pi w_0} = \sqrt{\frac{\lambda}{\pi z_R}}. \tag{1.20}$$

The divergence angle is also associated with the numerical aperture of the beam, similar to the concept used in imaging. This treatment is valid as long as the beam is paraxial, and justifies the approximations made. This analysis is for divergence angles below about 0.5 rad, or about 30 degrees. More intuitively, this condition means that the beam width has to be much larger than the wavelength.

We can also see that the divergence of the beam is consistent with diffraction. For example, the divergence of the first diffraction minimum from a circular aperture of radius a when it is illuminated by a plane wave is given by

$$\theta = \frac{1.22\lambda}{2a}.$$

In our case we could visualize the waist of our optical beam as a fuzzy Gaussian aperture of radius w_0.

In "ordinary" situations we have that the following relation holds

$$\lambda \ll w_0 \ll z_R. \tag{1.21}$$

Let's do a numerical example: if we have a HeNe laser beam ($\lambda = 632.8$ nm) that is focused to a spot $w_0 = 0.5$ mm, the Raleigh range comes out to be $z_R = \pi w_0^2/\lambda = 1.2$ m. In examining Eq. 1.15, we see that as w_0 decreases, z_R decreases more rapidly, so that as w_0 approaches λ, z_R approaches w_0. Efforts to produce 3-dimensional imaging with confocal microscopes relies on creating the conditions where both w_0 and z_R are small, and filtering the light with apertures.

6 | Complex Light Beams

1.2.1.2 Beam intensity

The explicit expression for the amplitude is

$$U_0 = \sqrt{\frac{2}{\pi}}\frac{1}{w}e^{-r^2/w^2}, \tag{1.22}$$

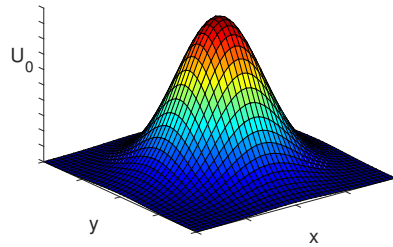which in the transverse plane has the typical Gaussian profile, as shown in Fig. 1.2.

Figure 1.2.   A 3-D view of the magnitude of the amplitude of the fundamental Gaussian beam as a function of the transverse coordinates.

The irradiance of the beam is defined as the energy per unit area per unit time delivered by the beam on a surface. It is given by

$$I = \frac{c\epsilon_0}{2}(E_0 U_0)^2, \tag{1.23}$$

If we integrate the irradiance, we get the total power of the beam:

$$P = \int_0^\infty I\, 2\pi r dr = \frac{c\epsilon_0}{2}E_0^2. \tag{1.24}$$

It is usual to know the total power of a beam because it can be measured easily with a power meter. By combining the previous equations we can express the irradiance of the beam in terms of the total power of the beam:

$$I = \frac{2P}{\pi w^2}e^{-2r^2/w^2}. \tag{1.25}$$

Should we send the beam through a circular aperture of radius a, the transmitted power will be

$$P_a = P\left(1 - e^{-2a^2/w^2}\right). \tag{1.26}$$

If we set $a = w$, we will get 86% of the light through, and if we set $a = \pi w$, we will get 99% of the light through.

At $r = 0$ the dependence of the amplitude with z is given by $1/w$. From the analysis of w in the previous section we gather that for $z < z_R$ the intensity is nearly constant, but for $z \gg z_R$, since $w \propto z$, the intensity decreases as $1/z^2$.

1.2.1.3 Wavefront

The wavefront is normally referred to the surface that contains the points of equal phase. The first phase term of Eq. 1.18, $\exp[i(kz - \omega t)]$, represents the phase of a plane wavefront perpendicular to z. All alone, it would represent a plane wave. The next phase term, $\exp(ik(x^2 + y^2)/2R)$ represents a correction to the planar phase front, reflecting the expansion of the beam. It has the same variation as that of a spherical surface of radius R. However, per Eq. 1.16, R depends on z: at $z = 0$ the radius of curvature is $R = \infty$ (i.e., a vertical plane, as shown in Fig. 1.1.). When $z \gg z_R$ then the radius of curvature is $R(z) \simeq z$, carrying the phase a spherical surface traveling away from $z = 0$. A special point is $z = z_R$, where the radius of curvature is $R = 2z$. This distance is also known as the confocal parameter. It is important for many problems in laser-beam optics such as in designing laser resonators. In these cases the laser medium is put in between two spherical mirrors of radius of curvature equal to their separation.

1.2.1.4 Gouy phase

The last phase term in Eq. 1.18 is almost always overlooked or not even mentioned in basic treatments in optics, but it is important in understanding complex light beams. It is the Gouy phase, given by Eq 1.17. It is a phase that arises due to diffraction. The warping of the wavefront from $z = 0$ to $z \gg z_R$ comes at a cost: an additional phase is accrued by the light wave. The accumulated Gouy phase can be as high as π from end to end when focusing a beam (and higher for high-order beams, as discussed below). However, it is an overall phase, so if the beam is not interfering with another beam coherent with it, this phase has no effect.

Fig. 1.3. shows a graph of the Gouy phase, which depends on the propagation coordinate. This phase changes rapidly between $z = -z_R$ and
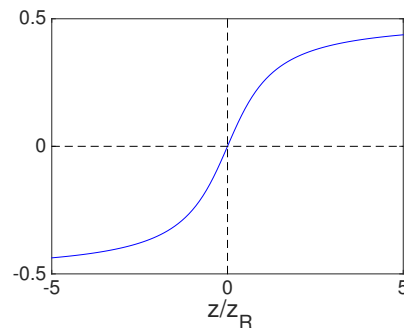

Figure 1.3.   Graph of the Gouy phase $\varphi(z)/\pi$.

$z = +z_R$, and reaches asymptotes $\pm\pi/2$ when $|z| \gg z_R$.

1.2.1.5 Momentum

A photon of light has an energy given by

$$E = h\nu, \tag{1.27}$$

where h is Plank constant and ν is the frequency of the light. A beam of light with a wavelength of 500 nm consists of photons, each with an energy of 4×10^{-19} J. Thus the number of photons traveling in a beam of power P is

$$N = P/E, \tag{1.28}$$

which for 500-nm light translates into 2.5×10^{15} per second. At the same time, a photon also carries a linear momentum of

$$p = E/c, \tag{1.29}$$

where c is the speed of light. The momentum for a photon of wavelength 500 nm is 1.3×10^{-27} kg m s^{-1}, which is quite small to make a visible effect on a macroscopic object. However, on a microscopic object light can exert a significant force. A particle that absorbs all of the light incident upon it will experience a force

$$F = Np, \tag{1.30}$$

which for the photon of our example is 3.3 pN. This force is greater than the weight of a 5-μm plastic sphere: 0.67 pN.

The realization of these magnitudes and the wide-spread use of lasers has led to the development of optical tweezers, which can trap and move micron-sized objects in a small sample, such as a microscope slide. Moreover, when light is focused on transparent objects they refract the light, changing its direction, and thus receiving a recoil force. This situation is so fortunate that a transparent object immersed in a liquid of distinct index of refraction can be trapped at the waist of a focused beam of light [4, 41]. This is shown schematically in Fig. 1.4.: two rays aimed above the center of a transparent sphere refract. In doing so, the initial momentum of the rays, p_i, leaves the sphere with a final momentum p_f. The change in the momentum of the light, Δp, results in a recoil momentum of the sphere p_{recoil} that pushes the sphere toward the focus of the light. This is the principle of optical tweezers [33]. The previous argument is the one that is most appropriate for objects of size greater than about a micrometer. For smaller-size spheres a better approach is one that treats the sphere as a radiating dipole, and its interaction with the light leads to a potential energy gradient that pulls objects to the focus of the light [49].

Figure 1.5. shows images of a sphere trapped in an optical tweezer setup. Frames (a), (b) and (c) show the motion of the labeled sphere through a sample with other spheres. The sideways motion can go as fast the trap can overcome the viscous drag force[47]

$$F_{\mathrm{drag}} = 6\pi\eta a v, \tag{1.31}$$

where a is the radius of the sphere (2.5 μm), v the velocity of the sphere (5 μm/s) and η the viscosity (of water, 0.001 Pl), which results in a magnitude of 0.24 pN. The three-dimensional aspect of the trap is observed in the frames (d), (e) and (f), where the sample was moved in and out of focus while the trapped sphere remained in focus. Gaussian beams have had a huge impact in biomedical research via the manipulation of subjects under the microscope, in the device known as optical tweezers. [41, 32]
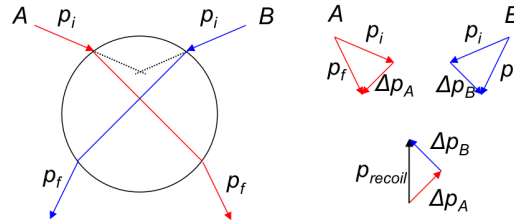
Figure 1.4.   Diagram of light rays, refracted by a sphere showing how the change in momentum of the light translates into a recoil of the sphere toward the focus of the rays.
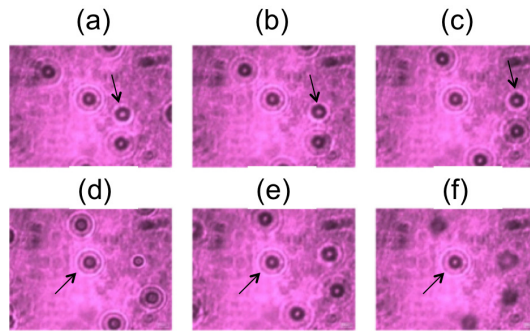

Figure 1.5.   Images of latex spheres trapped in optical tweezers. Frames (a)-(c) shows the effect of lateral trapping via the motion of the trapped sphere (marked by an arrow) relative to the field of other spheres in the sample. Frames (d)-(f) shows axial trapping of the labeled sphere, which remains in focus while the others go in and out of focus.

1.2.1.6 Gaussian-beam optics

It is important to mention that, unlike beams of light carrying images, Gaussian beams do not follow the simple rules of geometric optics such as the thin lens formulas. This is because Gaussian beams straddle a regime between a ray and wave. The correct treatment of propagation of Gaussian beams is given by the ABCD theory of Gaussian-beam propagation [40]. Because $q(z)$ and $p(z)$, of Eqs. 1.9 and 1.11, respectively, define the wave function of the light, we must follow the changes that those parameters incur during propagation. In this regard, it is instructive to realize that Eq. 1.10 can be rewritten as

$$\frac{1}{q} = \frac{1}{R} + i\frac{\lambda}{\pi w}, \tag{1.32}$$

which relates the real and imaginary parts of q to R and w. Thus to find the values of R and w along an optical system we only need to know how to find q as a function of z.

For propagation through free space between points z_1 and z_2, the transformation for q is given by

$$q_1 - z_1 = q_2 - z_2. \tag{1.33}$$

Thus, combining Eqs. 1.32 and 1.33 can lead to a method of obtaining R and w at all points starting from a given set of initial points. The effect of a lens on a Gaussian beam results in a change in the radius of curvature of the wavefront:

$$\frac{1}{R_2} = \frac{1}{R_1} - \frac{1}{f}, \tag{1.34}$$

where R_1 and R_2 are the radii of curvature of the wavefront before and after the lens, respectively, and f is the focal length of the lens. The sign convention for R is: positive when the center curvature is to the left, and negative when it is to the right. This is shown in Fig. 1.6. for a particular case where $R_1 > 0$ and $R_2 < 0$. It is easy to see that if the incoming beam on a converging lens of focal length f has a large radius of curvature (say $R_1 = \infty$), then the radius of curvature of the light after the lens is $R_2 = -f$. This seems to imply that the waist past the lens will be a distance R_2 from
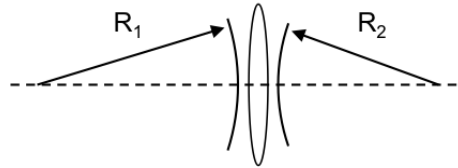

Figure 1.6.   Change in the radius of curvature of the wavefront by passage through a lens.

the lens. However, this is only true if $z_{R,2} \ll R_2$. Otherwise, we need to propagate q to the waist (i.e. where R is infinite and w is minimum). If we combine propagation with the effect of the lens, we find that the location of the waist is given by [42]

$$z_2 = \frac{R_2}{1 + [R_2\lambda/(\pi w_2^2)]^2}, \tag{1.35}$$

where w_2 is the beam spot of the beam just after the lens, which is the same as the beam spot just before the lens, w_1. The new waist is given by

$$w_{02} = \frac{w_2}{\{1 + [\pi w_2^2/(R_2\lambda)]^2\}^{1/2}}. \tag{1.36}$$

Notice that when

$$R_2 \ll \pi w_2^2/\lambda. \tag{1.37}$$

we get

$$z_2 \simeq R_2 \qquad (1.38)$$

and

$$w_{02} \simeq \frac{\lambda R_2}{\pi w_2}. \qquad (1.39)$$

Note that Eq. 1.37 is readily satisfied in situations where we want to focus a beam with a short focal length lens. For example, a visible laser beam with a width of 1 mm and a visible wavelength of 632 nm gives $\pi w_2^2 / \lambda \sim 5$m. If $R_1 \gg f$, then we only need $f \sim R_2$ to be less than a meter or so. In many applications we need to get the smallest waist possible. From Eq. 1.39 we get that what we need to do is to have the largest value of the input width w_2 and the smallest value for R_2. If the incoming beam has $R_1 \gg f$, then $R_2 \simeq f$, which implies that we need a lens with the shortest focal length possible. For other cases we need to apply the full formalism.

1.2.2 Hermite-Gaussian beams

In the previous section we found a solution to the paraxial wave equation by introducing a solution with an initial mathematical form. However, the final solution was "rigged" from the start: it was forced to be symmetric about the transverse plane. A more general solution would allow solutions with distinct dependencies on x and y coordinates. Thus, a more general trial solution is

$$U_0(x,y,z) = Ag(x,z)h(y,z)e^{\frac{ik(x^2+y^2)}{2q(z)}}e^{ip(z)}. \qquad (1.40)$$

The solution of the paraxial wave equation yields independent functions g and h that are Hermite polynomials [45]:

$$U_{m,n}(x,y,z) = \frac{A}{w}\mathrm{H}_m\left(\frac{\sqrt{2}x}{w}\right)\mathrm{H}_n\left(\frac{\sqrt{2}y}{w}\right)e^{-\frac{x^2+y^2}{w^2}}e^{\frac{ik(x^2+y^2)}{2R}}e^{-i\varphi(z)}. \qquad (1.41)$$

The constant term in Eq. 1.41 that normalizes the square of the amplitude is given by

$$A = \left(\frac{2^{1-N}}{\pi n! m!}\right)^{1/2}, \qquad (1.42)$$

and H_m and H_n are Hermite polynomials with (positive) integer indices m and n. Hermite-Gauss modes are often denoted as $\mathrm{HG}_{m,n}$. The order of the mode is given by

$$N = n + m. \qquad (1.43)$$

It is illustrative to see the expressions for the lowest-order Hermite polynomials $\mathrm{H}_m(v)$:

$$\mathrm{H}_0(v) = 1 \qquad (1.44)$$

$$\mathrm{H}_1(v) = 2v \qquad (1.45)$$

$$\mathrm{H}_2(v) = 4v^2 - 2 \qquad (1.46)$$

$$\mathrm{H}_3(v) = 8x^3 - 12x \qquad (1.47)$$
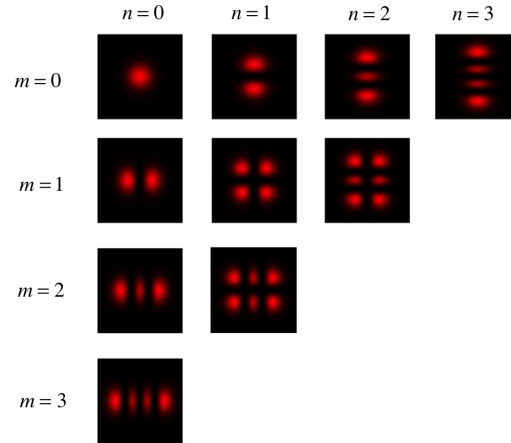
12 | Complex Light Beams

Figure 1.7. Graph of the irradiance of the lowest-order Hermite Gauss modes.

The product of the Hermite polynomials and the Gaussian term, in Eq. 1.41, result in the beam profiles shown in Fig. 1.7. Note that the zero-order $(N = 0)$ is the fundamental Gaussian mode. The indices m and n are also the number of zeros of the mode in the x and y coordinates, respectively. Thus, one can easily understand and predict the general shape of the mode from the values of m and n. One can also see that the size of the mode increases with the order. In laser resonators, modes of the same order are degenerate. Often laser resonators have an aperture within the laser cavity to eliminate these (unwanted) high order modes and lase only in the fundamental mode.

The phase terms of the mode are independent of the transverse coordinates. They are the same as those in Eq. 1.18 except for the Gouy phase, which in Eq. 1.41 has a new factor [9]:

$$\varphi(z) = (N + 1)\tan^{-1}(z/z_R). \tag{1.48}$$

If a beam is a superposition of modes, then propagation introduces a relative Gouy phase between the modes. Such a phase will affect the shape of the composite mode as the light propagates, especially if it is focused by lenses. Not all the points in the mode have the same phase, because the Hermite functions have positive and negative values. For example, inspection of the HG_{10} mode shows a node at $x = 0$, which correlates with H_1 in Eq. 1.45. Because H_1 has different sign for $x > 0$ and $x < 0$, the two lobes of HG_{10} are 180° out of phase. In fact, this is true with all adjacent lobes in Fig. 1.7. Figure 1.8. shows the amplitudes for two HG modes, illustrating the phase difference between adjacent lobes.

Hermite-Gaussian modes are best produced directly from an open-cavity laser by inserting fine crossed wires within the cavity. The laser modes that are generated will have nodes along the wires because scattering losses will
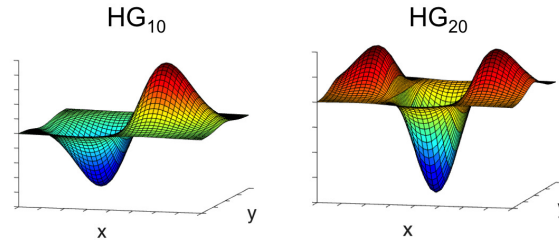
Figure 1.8.   Amplitude of Hermite-Gauss modes HG_{10} and HG_{20}.

discourage all other modes. This is easily done in any type of open-frame laser, such as gas lasers. The advantage of the method is that it is very efficient. The disadvantage is that higher-order modes do not lase with as high gain as low-order modes, so as the order of the generated mode goes up, the laser power in that mode goes down. Laser cavities with asymmetric frames or astigmatic gain regions can also be used to create mode superpositions and tailor a particular beam shape. Hermite-Gauss modes are of interest mostly for their connection to Laguerre-Gauss modes (described next) because the latter can be expressed as superpositions of Hermite-Gauss modes.

1.2.3 Laguerre-Gaussian beams

In the previous section we discussed a family of modes that appeared as solutions of the paraxial wave equation in Cartesian coordinates. If we choose a different coordinate system, such as cylindrical coordinates, we will get a new set of solutions. These solutions give rise to Laguerre-Gauss modes. These modes have very interesting properties, so we will subdivide this section into several parts.

1.2.3.1 Fundamentals

A first step is to set up the paraxial wave equation in cylindrical coordinates, and then allow the solutions to have independent solutions in terms of the transverse coordinates $r = (x^2 + y^2)^{1/2}$ (distance from the origin) and $\phi = \tan^{-1}(y/x)$, the angle about the transverse horizontal axis (x). The solution of the resulting equation is given by [2]

$$U_{p,\ell}(r, \theta, z) = \frac{A}{w} \left(\frac{\sqrt{2}r}{w} \right)^{|\ell|} L_p^{|\ell|} \left(\frac{2r^2}{w^2} \right) e^{-r^2/w^2} e^{ikr^2/[2R]} e^{i\ell\phi} e^{-i\varphi}, \quad (1.49)$$

where p and ℓ are integer indices, with p being only positive, and so the order of the mode is given by

$$N = 2p + |\ell|. \tag{1.50}$$

The normalization constant is given by

$$A = p! \left(\frac{2}{\pi p!(|\ell| + p)!} \right)^{1/2}. \tag{1.51}$$

The solution contains the associated Laguerre function L_p^ℓ that depend only on r. The lowest-order associated Laguerre functions are given by

$$\mathrm{L}_0^{|\ell|}(v) = 1 \tag{1.52}$$

$$\mathrm{L}_1^{|\ell|}(v) = 1 + |\ell| - v \tag{1.53}$$

$$\mathrm{L}_2^{|\ell|}(v) = \frac{1}{2} \left[v^2 - 2(|\ell| + 2) + (|\ell| + 1)(|\ell| + 2) \right] \tag{1.54}$$

One of the main characteristics of the solution is that the amplitude has a pure radial dependence, so that the intensity profile of the beams consists of one or more rings, as shown in Fig. 1.9. Indeed, the index p specifies the
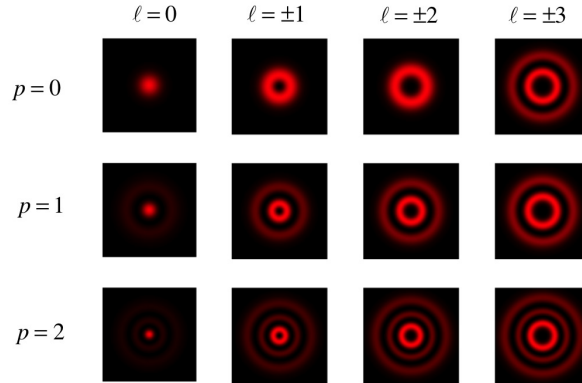

Figure 1.9.   Graph of the irradiance of the lowest-order Laguerre Gauss modes.

number of radial nodes. Because of the term of the form $r^{|\ell|}$, only when $\ell = 0$ there is a central maximum. For other values of ℓ the central spot is dark. When $\ell \neq 0$ and $p = 0$ the beams have a characteristic single-ringed "doughnut" shape, with the radius of the doughnut given by

$$r_\ell = \sqrt{\frac{|\ell|}{2}} w, \tag{1.55}$$

and a maximum amplitude at that radius that decreases monotonically with increasing $|\ell|$. The dark interior of Laguerre-Gauss modes also makes them amenable to imaging. In particular, it has been used in STED microscopy for high-resolution imaging [50, 28].

The most interesting term of Eq. 1.49 is the one where the phase varies as $\ell\phi$. It specifies that the phase of the wave that depends on the angular coordinate ϕ, and which winds ℓ-times-2π per revolution about the center of

the beam. The constant ℓ is known as the topological charge. This is illustrated in in the color-coded phase maps of the modes, shown Fig. 1.10. The center of each of the phase plots has a phase singularity or optical vortex. Since that point has all the phases, then the light interferes with itself
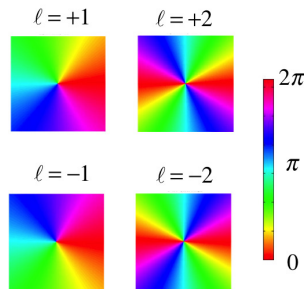

Figure 1.10.   False-color maps of the phase of the first- and second-order Laguerre-Gauss modes $p = 0$.

destructively, explaining the dark spot at the center of the beams. This aspect of Laguerre-Gauss modes has been the subject of much research [1].

The central spot containing the optical vortex is particularly sensitive to perturbations, so that when the beam is not in a pure mode but in a superposition, it is likely that the exact position of the optical vortex will be affected. When $|\ell| > 1$, any perturbation will split the vortex of charge ℓ into ℓ singly charged vortices [6].

1.2.3.2 Interference

There are other phase terms in the solution of Eq. 1.49, such as the curvature of the wavefront and the Gouy phase. The latter now follows the definition of Eq. 1.48, but with the order N given by Eq. 1.50. In this way, Hermite-Gauss and Laguerre-Gauss modes are very similar. If we interfere Laguerre-Gauss beams, one gets patterns such as those shown in Fig. 1.11. Frames (a) and (d) show respectively the modeled and measured the interference patterns for the case of two modes with $\ell = 1$ and $\ell = 0$ interfering collinearly. As can be seen, it is an asymmetric pattern. For higher values of ℓ the pattern consists of $|\ell|$ maxima symmetrically distributed about the center of the beam. If the relative phase between the modes is varied, the pattern rotates about the center of the beam. We can understand this the following way: the mode has a phase

$$\psi_\ell = \ell\phi \tag{1.56}$$

while the other mode has a constant phase ψ_0. We get constructive interference when

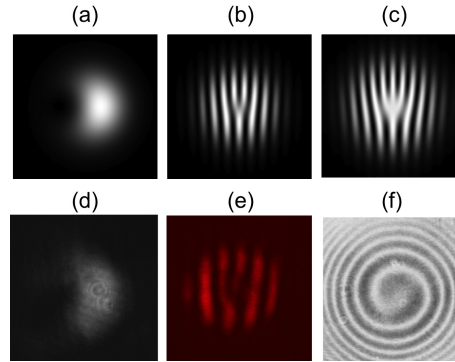$$\psi_\ell - \psi_0 = 2\pi n, \tag{1.57}$$

Figure 1.11.   Modeled interferograms of $\ell = 1$ and $\ell = 0$ modes interfering (a) collinearly, and (b) at an angle; and (c) of $\ell = 2$ and $\ell = 0$ interfering at an angle; measured interference pattern of $\ell = 1$ and $\ell = 0$ beams (d) collinearly (taken by P. Crawford), and (e) at an angle (taken by K. Beach); and (f) collinear interference of $\ell = 1$ with an expanded $\ell = 0$ beam (taken by H. Sztul).

where n is an integer. This will occur at angles

$$\phi_n = \frac{2\pi n + \psi_0}{\ell}. \tag{1.58}$$

If the phase of the zero-order mode changes, then the angle at which the n-th maximum occurs will rotate about the center of the beam. Note that for higher values of ℓ the pattern as a whole will rotate at a slower rate. If we change the sign of ℓ the pattern will rotate in the opposite sense for the same change in the relative phase.

Non-collinear interference gives rise to peculiar fringe patterns. Because of the optical vortex in these modes, which is a phase dislocation, the fringe interference pattern has a distinctive forked pattern. If the zero order mode forms an angle β, then its phase varies along the plane that contains both beams. Let us call that the coordinate x, and assume that the initial phase is ψ_0 at $x = 0$ The phase difference between the two modes on a screen in the x-y plane centered on the beam's intersection is given by [7]

$$\Delta\psi = \ell \tan^{-1}\left(\frac{y}{x}\right) - \frac{2\pi}{\lambda} x \sin\beta - \psi_0 \tag{1.59}$$

where we have expressed the variable ϕ in terms of the x and y coordinates. The graph of $\Delta\psi = 2\pi n$ gives rise to a forked pattern. The number of tines in the fork is the value of $|\ell| + 1$, as shown in Fig. 1.11.(b) and (c) where the interference pattern has been modeled for the cases $\ell = 1$ and $\ell = 2$, respectively. Thus, the interference pattern can be used to diagnose the topological charge of the beam. Figure 1.11.(e) shows the measured forked pattern. If the charge is negative, then the fork points in the opposite direction (down for the cases of the figure).

If the $\ell = 0$ beam is collinear but has a radius of curvature that is different broom the one of the beam carrying the optical vortex, then the phase difference between the two modes is

$$\Delta\psi = \ell\phi + \frac{2\pi r^2}{\lambda}\frac{1}{2R_0} - \psi_0, \tag{1.60}$$

where we have assumed for simplicity that $R_\ell \sim \infty$. If we require $\Delta\psi = 2\pi n$ we get a relation between r and ϕ corresponding to ℓ-intertwined spirals. Figure 1.11.(f) shows the measured pattern for the case with $\ell = 1$. As ψ_0 is changed the spiral pattern rotates.

1.2.3.3 Angular momentum

If we ignore phase due to the curvature of the wavefront and the Gouy phase, then he phase of the wave is given by the z and ϕ dependencies, or

$$\psi(r, \phi, z) = kz + \ell\phi. \tag{1.61}$$

This phase function follows the form of a helix of pitch λ. Points of equal phase, known as the wavefront of the beam, make ℓ-intertwined helices. This is shown in Fig. 1.12. for the cases with $\ell = +1$ and $\ell = +2$. The angular phase of the mode brings with it a new property of light beams: orbital angular momentum [2]. Fundamental light beams are known to carry linear momentum associated to their planar wavefront. Helical beams, such as Laguerre-Gauss with $\ell \neq 0$ carry angular momentum. This angular momentum depends on the rate of change of the phase with the angular coordinate, so it increases with $|\ell|$.
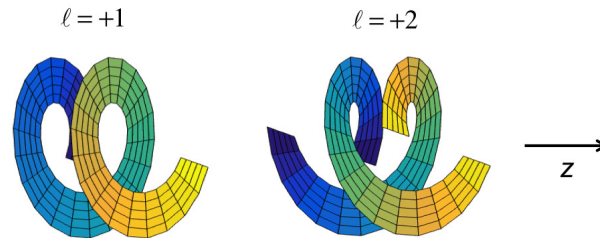

Figure 1.12.   A pictorial view of the wavefronts of beams with $\ell = +1$ (left) and $\ell = +2$ (right).

Each photon in a Laguerre-Gauss mode carries an angular momentum [2]

$$L = \ell\hbar, \tag{1.62}$$

where $\hbar = h/2\pi$, with h being Plank's constant. Because the waveform is tilted on one side of the beam and tilted the other way on the opposite side,

Laguerre-Gauss beams can exert torques on objects, especially irregular ones. To a fully absorptive particle the torque is given by [29, 41]

$$\tau = \frac{\ell P}{\omega}, \qquad (1.63)$$

where P is the absorbed power and ω is the angular frequency of the light. A sphere will rotate with an angular frequency given by

$$\Omega = \frac{\tau}{8\pi \eta a^3}. \qquad (1.64)$$

Figures 1.13.(a)-(c) show the rotation of a partially absorptive sphere effected by light in an LG_0^2 mode. The rotation of the irregular features of the sphere demonstrates its rotation.

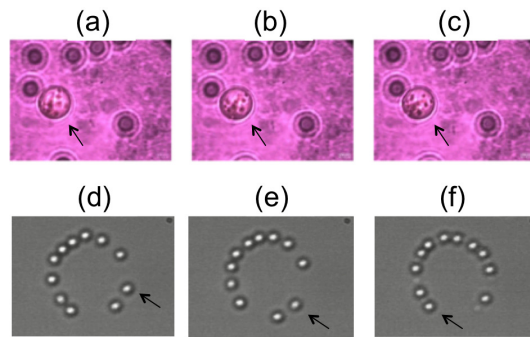Figure 1.13.   (a)-(c) Images of a 10-μm sphere (labeled) rotated in place by light with $\ell = 2$ (taken by N. Zehlev); (d)-(f) images of latex spheres moved along the ring of light with $\ell = 20$ (courtesy of M.J. Padgett). The arrow marks the same sphere.

When the objects are transparent but irregular, say cylindrical, the asymmetry of the objects changes the mode, as seen in the next section, which involves an exchange of angular momentum between the light and the object. In that case too the object will experience a torque. In addition to rotating objects in place, when the objects are small they get trapped by the intensity gradient along the ring of the mode, and because the wavefront is slanted along the ring, the objects will move along it, as seen in Figs. 1.13.(d)-(f).

1.2.4 Relations between mode families

Because Hermite-Gauss and Laguerre-Gauss functions each form a complete set, any mode can be expressed as a superposition of modes of either set, and in particular, the modes of one family can be decomposed into a superposition of modes of the other family. Moreover, the modes of a given

order N of one family have a decomposition in terms of a superposition of modes of the same order in the other family [9].

The connection between first-order modes is very illustrative. According to Eq. 1.41, the first-order Hermite-Gauss modes are given in abbreviated form by

$$HG_{10} = B_1 x \, G \, W \tag{1.65}$$

$$HG_{01} = B_1 y \, G \, W,, \tag{1.66}$$

where

$$B_1 = \frac{2\sqrt{2}}{\sqrt{\pi}w^2} \tag{1.67}$$

is a constant,

$$G = e^{-r^2/w^2} \tag{1.68}$$

is the Gaussian envelope, and

$$W = e^{-ikr^2/(2R)-i\varphi}, \tag{1.69}$$

is an overall phase term. In a similar way we can define the first-order Laguerre-Gauss modes:

$$LG_0^{+1} = A_1 r e^{i\phi} \, G \, W \tag{1.70}$$

$$LG_0^{-1} = A_1 r e^{-i\phi} \, G \, W \tag{1.71}$$

where

$$A_1 = \frac{2}{\sqrt{\pi}w^2} \tag{1.72}$$

is the normalization constant.

Notice that $A_1 = B_1/\sqrt{2}$. The Laguerre-Gauss modes can also be expressed as

$$LG_0^{\pm 1} = A_1 (x \pm iy) \, G \, W \tag{1.73}$$

or equivalently,

$$LG_0^{\pm 1} = \frac{1}{\sqrt{2}} (HG_{10} \pm iHG_{01}), \tag{1.74}$$

The previous equation means that the superposition of the two first-order Hermite-Gauss modes with a relative phase of $\pi/2$ give rise to a first-order Laguerre-Gauss mode. This type of relation can be easily realized in the laboratory, but more interestingly, it can be used, in combination with the Gouy phase, to convert first order modes of one family to the other. To understand this we first have to realize a relation between rotated Hermite-Gauss modes:

$$HG_{10}(\theta) = HG_{10}\cos\theta + HG_{01}\sin\theta, \tag{1.75}$$

where θ is the angle that mode HG_{10} is rotated. In particular, when $\theta = \pi/4$ one gets

$$HG_{10}(\pi/4) = \frac{1}{\sqrt{2}} \left(HG_{10} + HG_{01} \right). \tag{1.76}$$

That is, the superposition of the two Hermite-Gauss modes in phase gives rise to the mode rotated by $\pi/4$. Note the similarity between Eqs 1.74 and 1.76. If we have a way to introduce a phase of $\pi/2$ between the two Hermite-Gauss modes we convert a rotated Hermite-Gauss mode into a Laguerre-Gauss mode. This can actually be done with optical components using the Gouy phase and cylindrical lenses; a device known as a mode converter [9]. The idea is that a cylindrical lens introduces a Gouy phase in one dimension but not the other, so modes aligned with the axis of the cylindrical lens will experience a Gouy phase that is different than the mode aligned with the axis perpendicular to the cylindrical lens. This is shown in Fig. 1.14. The combination of two spherical and two cylindrical lenses results in creating a phase of $\pi/2$ between the modes parallel and orthogonal to the cylindrical axes. By inputting a mode oriented at $\pi/4$, per Eq. 1.76, it is decomposed into the modes parallel and perpendicular to the astigmatic axis of the mode converter. The latter introduces a $\pi/2$ phase between them via the Gouy phase. The resulting mode is then a Laguerre-Gauss mode.
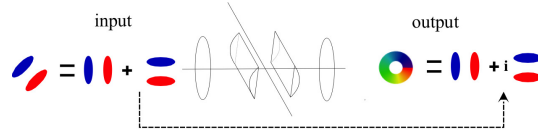

Figure 1.14.   A $\pi/2$ mode converter.

Hermite-Gauss modes do not carry orbital angular momentum. Because the mode converter converts a Hermite-Gauss mode into a Laguerre-Gauss mode, the light exchanges angular momentum with the apparatus. In the case of optical tweezers, irregular objects can exchange angular momentum with the light, and thus receive a recoil torque.

The two first-order Hermite-Gauss modes can also be put in terms of the two first-order Laguerre-Gauss modes:

$$HG_{10} = \frac{1}{\sqrt{2}}(LG_0^{+1} + LG_0^{-1}) \tag{1.77}$$

$$HG_{01} = \frac{-i}{\sqrt{2}}(LG_0^{+1} - LG_0^{-1}). \tag{1.78}$$

The zero orders are the same for the two families: $LG_0^0 = HG_{00}$. These relations between families can be extended to higher orders [9]. For example,

$$LG_0^{+2} = \frac{1}{2}HG_{02} - \frac{i}{\sqrt{2}}HG_{11} - \frac{1}{2}HG_{20} \tag{1.79}$$

$$LG_0^{-2} = \frac{1}{2}HG_{02} + \frac{i}{\sqrt{2}}HG_{11} - \frac{1}{2}HG_{20} \tag{1.80}$$

$$LG_1^0 = \frac{1}{2}HG_{02} + \frac{1}{2}HG_{20} \tag{1.81}$$

The converse relationship can be deduced from the previous. One final case of importance is that of the cosine form of the Laguerre-Gauss mode:

$$LGc^{|\ell|} = \frac{1}{\sqrt{2}}(LG_0^{\ell} + LG_0^{-\ell}) \tag{1.82}$$

which is a symmetric mode with $2|\ell|$ lobes symmetrically arranged about the center of the beam. A relative phase between the two only rotates the pattern.

Finally, there exist a distinct but related family of modes, known as Ince-Gaussian beams [5]. They provide a continuous transition between Laguerre-Gauss and Hermite-Gauss modes.

1.2.5 Laboratory methods of production

Low-order Hermite-Gauss modes can be produced directly by lasers bearing apertures or obstacles to encourage maximum gain for a particular mode and too much loss for all the other modes [9]. This is not so easy for Laguerre-Gauss modes because it is not straightforward to enhance one topological charge ℓ and discourage the mode with $-\ell$. Thus, Laguerre-Gauss modes are mostly produced externally via mode transformation. In the previous section we mentioned a method that uses mode converters to transform Hermite-Gauss modes into Laguerre-Gauss modes. That method is a good one for a few set of low-order modes.

1.2.5.1 Spiral phase plate

Higher-order Laguerre-Gauss modes can be produeed via spiral phase plates, sometimes called vortex lenses. These devices are also available commercially. They consist of a glass substrate that has a dielectric deposited over it in the shape of a helical ramp. This ramp retards the light through its angle-dependent thickness, shown schematically in Fig. 1.15.(a). The step is of a height that leads to delaying the wave from either side of the step by an integer number of wavelengths. In particular, If the medium of the ramp has an index of refraction n, and the step has a height h, then the at either side of the step the light acquires a phase $\phi_+ = 2\pi nh/\lambda$ and $\phi_- = 2\pi h/\lambda$ (assuming air is the surrounding medium). For a Laguerre-Gauss mode of order ℓ the difference in phase at either side of the step is $\phi_+ - \phi_- = 2\pi\ell$. Therefore, the height of the step is

$$h = \frac{\ell\lambda}{n-1}.$$ \hfill (1.83)

There are experimental challenges to creating the sharpest step, but the greatest challenge is to produce a pure mode. Let us assume that the phase plate has no imperfections, then sending a Gaussian beam through it will produce a mode with topological charge ℓ, but not in a $p = 0$ mode, but in a superposition

$$\mathrm{LG}^\ell_{\mathrm{sup}} = \sum_{p=0}^{\infty} c_p \mathrm{LG}^\ell_p$$ \hfill (1.84)

where c_p is a coefficient that will be greatest for $p = 0$ and decrease in magnitude for higher values of p. The resulting mode may even resemble a singly-ringed $p = 0$ mode, but its radius will not correspond to what one may
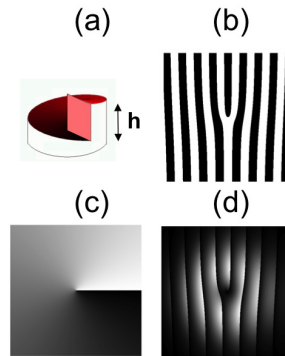
Figure 1.15.   Diffractive elements to produce Laguerre-Gauss modes: (a) spiral phase plate; (b) binary forked grating; (c) phase pattern for producing $\ell = 1$ modes with an SLM on reflection or transmission; (d) amplitude-modulated phase-blazed pattern for producing $\ell = 1$ modes with an SLM by diffraction.

predict via the equations outlined in sections above. The reason is quite simple: the light going through the center of the spiral phase plate has all phases, so it undergoes destructive interference. A few wavelengths away past the plate, the light beam already has a dark spot, but the light that initially was at the center of the input mode has to go somewhere, so diffraction takes care of it. The final mode is a multi-ringed mode with topological charge ℓ. In many applications this is still acceptable, but in applications where one requires a pure mode, then the light that enters the phase plate has to already have the proper ringed-shaped intensity. That is, for producing the purest mode we need to apply phase and amplitude modulation.

The analogous device for a Hermite-Gauss mode is a stepped phase plate. The adjacent lobes of all Hermite-Gauss modes are π out of phase, so a plate that shifts the phase by the right amount can also be used. In first-order modes where the there are only two lobes, a simple piece of glass of the proper thickness, or tilted for fine adjustment, can be used to generate them from an incoming fundamental Gaussian mode. The method still brings the diffractive effects as with the spiral phase plate: the lack of amplitude modulation creates additional lobes.

1.2.5.2 Holographic diffraction

By far the most efficient and versatile method of producing high-order modes is through the use of diffractive optical elements. These come in two forms: passive and active. Passive gratings can be holographic, engraved, or binary. Active ones can use liquid-crystal-based electronic devices, such as a spatial light modulator (SLM) to dial the desired pattern on demand.

The simplest diffractive device is the binary grating, an amplitude grating that either blocks or transmits light. It is generated simply by taking a black and white photograph of the diffraction pattern and using the developed negative as the diffraction grating [30]. Figure1.15.(b) shows an example of a binary grating pattern with a dislocation charge $q = 1$. Diffracted orders will have a topological charge that increases with the order. The incident beam can also have a topological charge ℓ_{inc}. In general the m-th diffractive order will have a topological charge.

$$\ell_{\mathrm{diff}} = \ell_{\mathrm{inc}} + mq. \tag{1.85}$$

The most important problem of the binary grating is its efficiency. It is partially opaque and the diffraction efficiency is low. Despite this, many early research on complex light problems were done using this method. A better approach is to use a phase-blazed grating. For a passive device, this requires it to be holographic [36]. The photographic diffractive element is challenging to fabricate. The easy alternative today is provided by a modern electro-optic device brought in by the computer display industry: the SLM. This device uses a liquid crystal medium to act as a pixelated birefringent device, imparting an electronically addressable space-variant retardance on the light that passes through it. Thus, these devices allow one to dial-in the desired light mode by phase sculpturing it. They can also be highly efficient. They can be used in two distinct modes: on reflection/transmission, and on diffraction. The gray-scale encoded pattern for the former is shown in Fig. 1.15.(c). It is the pattern that gets programmed onto the SLM, and where the gray level becomes a phase shift imparted onto the light, and where white is, say, phase zero and black is phase 2π. The pattern of the figure was generated by encoding in gray scale the phase of Eq. 1.60 modulo-2π, with $R = \infty$, $\ell = 1$, $\psi_0 = 0$ and r and ϕ specifying SLM pixels. This is the electronic form of the spiral phase plate, where the phase delay is imparted by the birefringence of the SLM instead of a pathl through a refractive medium of varying thickness.

The spiral patterns encoded onto the SLM have the same shortcomings of the spiral phase plate. The alternative is to generate the modes on diffraction. To resolve the problem of efficiency, the pattern of the grating is blazed, and to resolve the problem of mode purity, the grating is amplitude modulated [13]. An example of such a pattern is shown in Fig. 1.15. for the case of $\ell = 1$. In this case, Eq. 1.59 was used, modulo-2π, and multiplied by a modulation factor related to the shape of the mode. The combination of amplitude phase modulation allows one to engineer a pure mode. The SLM has other advantages: the phase can also be manipulated to include deliberate mode superpositions and to simulate other optical elements such as lenses and astigmatic elements [34].

1.3 Non-Diffracting Optical Beams

The previous sections were devoted to beams of light that are solutions of the wave equation, and which suffer from diffraction: as the beam propagates,

they evolve by expanding and phase-shifting via the Gouy phase. New and distinct types of beams have been studied and developed that, through a finite region of space, preserve their size and shape unaltered. That is, beams that temporarily do not diffract. Some may even say that they are a 3-dimensional interference pattern, but one that remains intact for a design distance. We also saw that the concept of a pure mode is meaningful within a mathematical framework, because a pure mode in one family, say Laguerre-Gauss, is a superposition (and consequently an interference beam) of pure modes of another family, such as Hermite-Gauss. Even a fundamental Gaussian beam can be thought of an infinite superposition of plane waves. The case of non-diffracting light beams is fascinating for its simplicity and elegance, and for their unique properties. In this section we will discuss two distinct types of non-diffractive beams: Bessel beams and Airy beams. In both cases, the ideal function is of infinite extent, as are plane waves, but implementations of truncated functions still show the same ideal properties for finite and but not insignificant regions of space.

1.3.1 Bessel Beams

The best way to understand Bessel beams is by starting with how they can be made, shown in Fig. 1.16.(a). A beam of light with a planar wavefront is incident on an axicon. This is a conical optical element: a prism of revolution. It is flat on one side (facing the incoming light) and conical on the other side. It is normally characterized by its apex or opening angle α. Figure 1.16.(a) shows a section of the axicon that includes its axis; a view where the axicon looks like a prism. A more convenient angle is base angle, shown in the figure, and related to the apex angle by

$$\gamma = \pi/2 - \alpha/2, \tag{1.86}$$

If the incoming rays are parallel to the axis, they are not refracted by the first surface. Refraction at the second surface yields, via Snell's law, the relation

$$n \sin \gamma = \sin(\theta + \gamma), \tag{1.87}$$

where θ is the angle that the refracted rays form with the z-axis, and n is the index of refraction. Incoming rays above the axis are refracted downward, and similarly, incoming rays the rays below the axis are refracted upward. This is of course the description of just the rays contained in the plane of the figure. All the refracted rays of a given input impact parameter w_0 (distance from the axis) form a three-dimensional cone after the axicon. For small angles, the refracted angle is given by

$$\theta = (n-1)\gamma. \tag{1.88}$$

The group of rays from the top overlaps with the ones from the bottom over a distance

$$z_{\max} \simeq \frac{w_0}{\theta}. \tag{1.89}$$
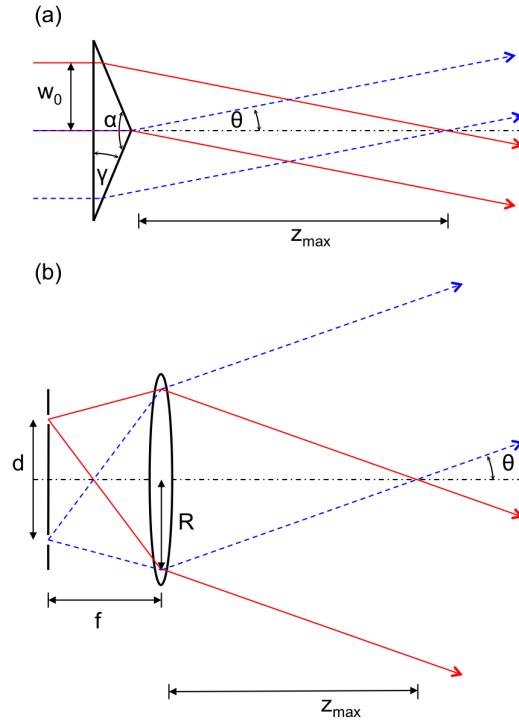
This quantity is also the depth of focus of the beam.

Figure 1.16.   Methods of production of Bessel beams: (a) with an axicon of base angle γ; and (b) with an annular slit of diameter d, and a lens of focal length f.

The beam that results can be thought of being made of a superposition of plane waves that have a wave number k forming an angle θ with the axis. These waves have a longitudinal component

$$k_z = k \cos \theta \tag{1.90}$$

and a radial (transverse) component

$$k_r = k \sin \theta. \tag{1.91}$$

A solution for the electric field within the region of overlap is [21]

$$E(r, \phi, z) = A_0 e^{ik_z z} J_0(k_r r) \tag{1.92}$$

where A_0 is a constant, the second term is the phase propagator associated with a plane wave traveling along the z-axis, and $J_0(k_r r)$ is the Bessel function of order 0. Notice that the magnitude of the mode depends only on r, and not at all on z. It means that in the region where the rays overlap, the magnitude of the field in the transverse plane remains constant. Thus, the

width of the beam does not change throughout the overlap region. For this reason, these beams are also known as non-diffracting. Figure 1.17. shows the intensity of the transverse profile. Note that a large fraction of the energy is concentrated in the central maximum of radius

$$r_0 = \frac{2.405}{r_4}, \tag{1.93}$$

which is the first zero of the Bessel function. For example, a glass axicon with a base angle $\gamma = 2.25°$ yields $\theta = 0.022$ rad, or $z_{max} = 46w_0$. If $w_0 = 7.5$ mm, then $z_{max} \sim 340$ mm. The radius of the central maximum for $\lambda \sim 600$ nm is 10 μm. A Gausian beam with a waist of the same value will expand due to diffraction and have a half-width of 6.5 mm at a distance $z = z_{max}$. This Bessel beam has huge depth of focus compared to that of the Gaussian beam: $2z_R = 1$ mm.
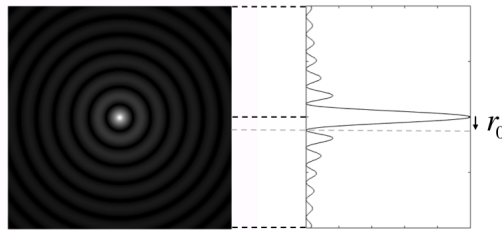

Figure 1.17.   Image of the transverse intensity of a zero-order Bessel mode and a graph of the zero-order function on an axis crossing the center of the mode.

Another simpler method of production of Bessel beams is shown in Fig. 1.16.(b) [22]. The beam is produced by a ring aperture and a lens. The ring has a diameter d and an aperture width Δd. Due to single-slit diffraction, the beam expands further after the ring. If the lens is placed a focal length f away from the aperture, it needs to have a minimum radius

$$R = \frac{d}{2} + \frac{\lambda f}{\Delta d}. \tag{1.94}$$

The second term accounts for the slit diffraction of the light up to the first minimum. The non-diffractive distance for this case is (for small angles)

$$z_{max} = \frac{R}{\theta}, \tag{1.95}$$

and where

$$\theta = \frac{d}{2f}. \tag{1.96}$$

The method, although inefficient (because most of the incoming light is blocked), is simple and inexpensive. To produce a Bessel mode with the same θ and z_{max} as the previous example, would require a ringed aperture with a

diameter of 13.2 mm, and a lens of 300 mm focal length with a 15-mm diameter. One can also understand this method of production in terms of Fourier analysis: the Bessel mode is the Fourier transform of the ring, a transform effected by the lens. Bessel beams can also be produced diffractively using either holograms [51], or spatial light modulators [18].

Beyond $z_{\max}$ the mode disappears, as there is no longer beam overlap or interference. Because these can be thin and non-expanding, they are particularly suited for imaging via scanning light-sheet microscopy.[23, 44] Bessel beams are "self healing" [38]. That is, an obstacle placed at a point along the beam does not cast a lasting shadow. Using simple geometry, we get that when a Bessel beam encounters an object of transverse side a, the mode repairs itself after a distance

$$z_{\mathrm{rep}} = \frac{a}{2\theta}. \tag{1.97}$$

The explanation is simple: the mode is produced by plane waves (rays) traveling at oblique angles, as shown in Fig. 1.16. Beyond z_{rep} the rays no longer hit the object, and so they recreate the beam as if the object was not there. In actual implementations there are deviations from the ideal modes described above, which can yield a z-dependent amplitude A_0 and other phase terms that may vary with z and r [35]. However, the pattern retains its constant Bessel shape as a function of z.

A Bessel beam with an azimuthal phase can be generated diffractively [52, 18], by using a high-order Laguerre-Gauss beam as input to an axicon [3], or by applying a phase delay around the aperture of the ring [53]. In this case the Bessel mode is given by

$$E_\ell = A_0 e^{ik_z z} e^{i\ell\phi} J_{|\ell|}(k_r r), \tag{1.98}$$

where now the Bessel function is a high-order one, with the order given by ℓ, the topological charge. The center will no longer be dark because it will carry an optical vortex. Other solutions to the wave equation yield non-diffracting solutions include Mathieu beams, which are elliptical realizations of Bessel beams [16].

1.3.2 Airy Beams

The Airy function is a one-dimensional function that is asymmetric about its coordinate, say x, which is oscillatory for $x < 0$ (extending out to infinity) and decaying exponentially for $x > 0$. It is a solution of a differential equation that appears in several physical situations, and especially in optics, around caustics [10]. In our case, implementations have involved a two-dimensional function that is the product of two one-dimensional Airy functions in orthogonal directions. If for now we concentrate on one direction, the Airy function appears as a solution of a paraxial one-dimensional wave equation [46], similar to Eq. 1.7:

$$\frac{\partial^2 U}{\partial x^2} + 2ik\frac{\partial U}{\partial z} = 0, \tag{1.99}$$

where $k = 2\pi/\lambda$. For $z = 0$ the solution $U(x, z)$ is simply the Airy function

$$U(x, 0) = \text{Ai}\left(\frac{x}{x_0}\right), \tag{1.100}$$

where x_0 is a scale factor. For $z > 0$ the solution is:

$$U(x, z) = \text{Ai}\left(\frac{x}{x_0} - \frac{z^2}{4k^2 x_0^4}\right) e^{i[xz/(2kx_0^3) - z^3/(12k^3 x_0^6)]}. \tag{1.101}$$

Note that the amplitude of the solution remains intact: only its argument changes, varying quadratically with z. That is, the pattern curves toward $x > 0$ as it propagates. More precisely, the beam describes a parabolic trajectory of the form

$$x = \frac{z^2}{2k^2 x_0^4}. \tag{1.102}$$

This motion is often referred as "acceleration," although the light does not follow a curved trajectory. It is the superposition (interference pattern) that curves. This trajectory follows the momentum which tilts the mode further as it propagates [48]. This one-transverse-dimensional version of the Airy beam has applications in light-sheet microscopy, producing a continuous sheet of non-diffracting light,[54] and at the same time relieving the need to scan the beam, as done in other forms of the technique.[44, 23]

A realization of this beam is recreated by truncating the function at the input ($z = 0$). It is also recreated in 2 dimensions, which results in a product of Airy functions of the x and y coordinates. However, the main features remain the same. The complete implementation has the modified form [14]

$$U(x, y, z) = \text{Ai}\left(\frac{x}{x_0} - \frac{z^2}{4k^2 x_0^4} - \frac{iaz}{kx_0}\right) \text{Ai}\left(\frac{y}{y_0} - \frac{z^2}{4k^2 y_0^4} - \frac{iaz}{ky_0}\right) \times$$
$$e^{ax/x_0 - az^2/(2k^2 x_0^4)} e^{i[(a^2 + x/x_0)z/(2kx_0^2) - z^3/(12k^3 x_0^6)]} \times \tag{1.103}$$
$$e^{ay/y_0 - az^2/(2k^2 y_0^4)} e^{i[(a^2 + y/y_0)z/(2ky_0^2) - z^3/(12k^3 y_0^6)]}$$

where $0 < a < 1$, and where $1/a$ is related to the transverse extent to the beam, similarly to the role of w for a Gaussian beam. There are two types of exponentials for each coordinate. The real exponentials produce an attenuation of the oscillatory part of the Airy beam in each dimension, x and y. The imaginary exponentials add coordinate-dependent phase factors. The latter result is the wavefront leading to the curvature of the beam.

Figure 1.18. shows three ways to view a two-transverse-dimension Airy beam. In Fig. 1.18.(b) we see the transverse image of the mode. The lobes correspond to the oscillations of the Airy function along the two coordinates. They show clearly the asymmetry of the function. The intensity as a function of x for $y = 0$ and $z = 0$ is shown in Fig. 1.18.(a). A different view is shown in Fig. 1.18.(c), which shows a contour-type graph of the intensity as a function of x and z for $y = 0$. The curvature of the graph clearly shows the acceleration of the beam. This feature appears due to the superposition of oblique plane waves, similar to the case of Bessel beams. For that reason, Airy beams also exhibit the self healing effect.
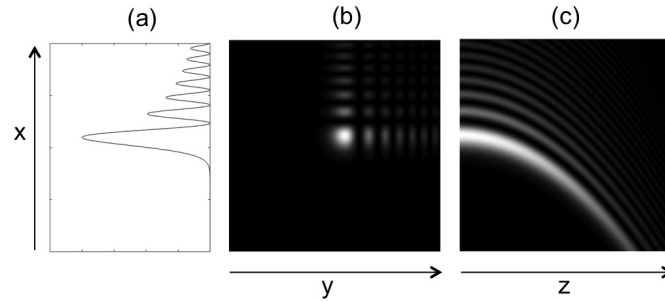
Figure 1.18.   Airy modes: (a) Intensity along the transverse coordinate x; (b) gray scale graph of the intensity in the transverse plane $x - y$; (c) gray scale graph of the transverse intensity along axes x and z for a one dimensional Airy beam.

1.4 Beams with Space-Variant Polarization

Previous sections covered scalar beams, where every point in the beam had the same polarization. That is, the vectorial part of the beam is the same for all points. Here we discuss beams of light where the state of polarization is not constant throughout the beam. We address these types of beams in three sections. A first section gives a brief introduction to polarization of light, and the following sections present two types of beams: vector and Poincaré beams.

1.4.1 Polarization

Electromagnetic waves consist of transverse oscillations of electric and magnetic fields, $\overrightarrow{E}$ and $\overrightarrow{B}$, respectively. The two vectors are orthogonal to each other, and their magnitudes are related by

$$E = cB, \tag{1.104}$$

Thus, it is convenient to express the light only in terms of the electric field, with the understanding that the magnetic part is proportional to it and orthogonal in direction. Another reason to consider is that matter normally interacts more strongly with the electric field component of the light. Although not discussed here, there are situations where the magnetic field and its interactions play an important role.

   In a plane-wave description of the light, the electric field of a propagating electromagnetic wave oscillates linearly in the plane that is transverse to the propagation. In linear polarization, the electric field oscillates in a single plane that contains the propagation direction. If we denote the state of linear polarization along the x-direction by $\hat{e}_x$, and similarly, for the linear polarization along y-direction by $\hat{e}_y$, then a general expression for the electric

field is a linear superposition of these two components [42]

$$\overrightarrow{E} = E_0 \left(\cos \alpha \ \hat{e}_x + \sin \alpha \ e^{-i2\delta} \hat{e}_y \right), \tag{1.105}$$

where α and δ are angular variables that specify the relative amplitude and phase between the two components. When $2\delta \neq 0, \pi$ the polarization is in general elliptical. That is, the tip of the electric field describes an ellipse in the transverse plane. The orientation of the semi major axis and its relation to the semi minor axis are non-trivially related to α and δ. For this reason we take a different approach to represent the fields.

If $2\delta = \pm\pi/2$ and $\alpha = \pi/4$, the linear states are of the same magnitude but out of phase by $\pi/2$, and the electric field rotates, with the tip of the vector describing a circle. This is known as circular polarization. Depending on whether the phase is positive or negative, the electric field rotates in one sense or the other, and so we call right and left circular polarization when the electric field rotates clockwise and counter clockwise, respectively, as a function of time in a given transverse plane when we are looking into the beam of light. The states of right (R) and left (L) circular polarization can be described in terms of the linear states as:

$$\hat{e}_R = \frac{1}{\sqrt{2}}(\hat{e}_x - i\hat{e}_y) \tag{1.106}$$

and

$$\hat{e}_L = \frac{1}{\sqrt{2}}(\hat{e}_x + i\hat{e}_y), \tag{1.107}$$

respectively. The complex factor is $i = \exp(i\pi/2)$ encodes the phase between the two components. Because $\hat{e}_R$ and $\hat{e}_L$ are orthogonal, we can express a general state of polarization in terms of them:

$$\hat{e} = \cos \chi \ \hat{e}_R + \sin \chi \ e^{-i2\theta} \hat{e}_L, \tag{1.108}$$

This state represents an ellipse with an ellipticity [17]

$$\epsilon = \tan(\pi/4 - \chi) = \pm\frac{b}{a}, \tag{1.109}$$

where b and a are the semi-minor and semi-major axes of the ellipse, respectively; and an orientation of the semi major axis θ. That is, in this representation the ratio of amplitudes of the two components determines the ellipticity and their relative phase specifies the orientation.

The Poincaré sphere of Fig. 1.19. is a convenient geometrical construction that allows us to represent all the states of polarization by points on the surface of the sphere [12]. Angle χ is half of the polar angle, and θ is half the azimuthal angle, or longitude on the sphere, as shown in Fig. 1.19.

The north and south poles are the states of right and left circular polarization, respectively. All the points along the equatorial line are states of linear polarization with orientations that depend on the azimuth angle. Points in between, in the northern and southern hemispheres are states of elliptical polarization with right and left handedness, respectively. The full array of states is shown in Fig. 1.20.
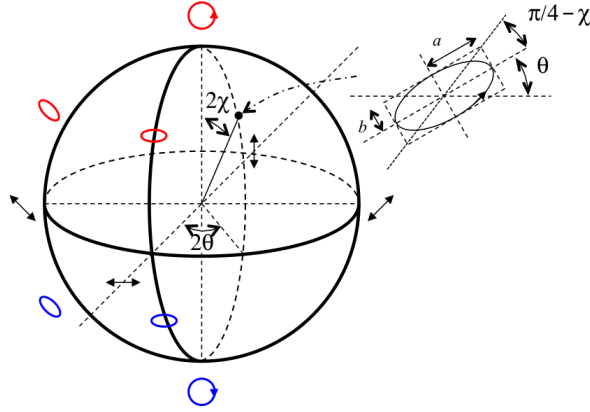
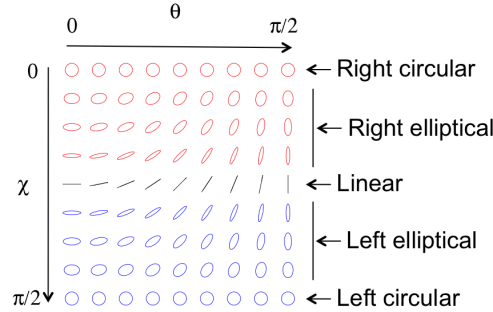Figure 1.19.   Poincaré sphere for mapping all states of polarization.

Figure 1.20.   Mapping of states of polarization via angles χ and θ.

1.4.2 Vector Beams

A class of these beams has only linear polarization, and are known as vector beams or modes. The most important vector mode is the radial mode. It is a mode where the state of polarization is linear but its orientation is radial, as shown in Fig. 1.21.(a). This mode can be understood easily as a superposition of two first-order Laguerre-Gauss modes in orthogonal states of circular polarization:

$$U = \frac{1}{\sqrt{2}} (LG_0^{+1} \hat{e}_R + LG_0^{-1} e^{-i\gamma} \hat{e}_L), \tag{1.110}$$

where γ is a phase. Replacing the expressions for the Laguerre-Gauss modes of Eqs. 1.70 and 1.71 into Eq. 1.110, and setting $\gamma = 0$ gives

$$U = \frac{1}{\sqrt{2}} A_1 r G W \left(e^{+i\phi} \hat{e}_R + e^{-i\phi} \hat{e}_L \right), \tag{1.111}$$

and where G and W are defined by Eqs. 1.68 and 1.69. Notice that the amplitudes get factored out, so the state of polarization is linear. Inside the parenthesis we have a superposition of circular states with a relative phase between them. Thus, the orientation of the resulting linearly polarized state, which is given by half the relative phase, depends only on the transverse angle: $\theta = \phi$. The vector mode can also be produced by a superposition of first-order Hermite Gauss modes:

$$U = \frac{1}{\sqrt{2}} \left(HG_{10} \hat{e}_x + HG_{01} \hat{e}_y \right). \tag{1.112}$$

This can be understood by analyzing the x and y dependencies of the expressions for the modes in Eqs. 1.65 and 1.66, and realizing that $x = r \cos \phi$ and $y = r \sin \phi$.

This state has been of interest because when focused by a lens, a longitudinal electric field appears at the center of its waist [24]. This mode is attractive because the waist is smaller than the one produced with uniform polarization [20]. When $\gamma \neq 0$, the orientation of the polarization is given by $\theta = \phi + \gamma/2$. When $\gamma = \pi$, the orientation is perpendicular to the radial dimension, or tangential, as shown in Fig. 1.21.(b).
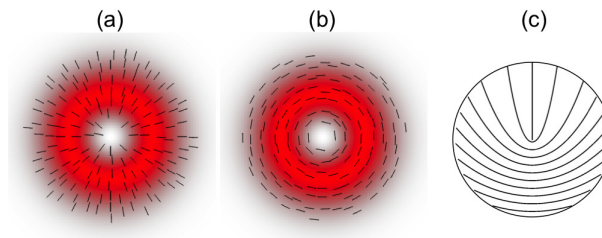

Figure 1.21.   Radial (a) and tangential (b) vector modes, where orientation of the linear state of polarization varies across the beam profile, denoted by lines. (c) pattern of fast axis orientations in a spatially-variable half-wave plate that gives rise to vector modes.

These vector modes can be made in several ways. One is by direct superposition of Laguerre-Gauss or Hermite-Gauss modes with an interferometer (see Refs. [55] and [26] for a review of previous methods). Another method involves using a specially designed optical element that acts as a half wave plate with a fast axis orientation that varies with the angular coordinate:

$$\alpha_{\text{fast-axis}} = q\phi \tag{1.113}$$

with $q = 1/2$. The pattern followed by the fast axes of the element is shown in Fig. 1.21.(c). Linearly polarized light entering a half-wave plate gets its orientation rotated by twice the angle that it forms with the fast axis. Thus, this device rotates incoming uniformly polarized light by an amount that depends on ϕ. The relative angle of the device as a whole with the incoming

polarization specifies the orientation of the light at each angle. In the case of Fig. 1.21.(c), incoming vertical polarization gives rise to radial polarization; and incoming horizontal polarization gives rise to tangential polarization. Devices like these can be made stitching standard birefringent materials cut into pie sectors, with each pie sector having its fast axis forming an angle given by Eq. 1.113 [20]. A continuously varying fast axis in a single element has been designed using liquid crystals, and is already available commercially. A particularly interesting device is known as a "q-plate" allows the fast-axis angle of the device (q in Eq. 1.113) to be tunable [37]. This also allows one to create beams like the ones discussed in the next section.

The superpositions of Eqs. 1.110 and 1.112 are non-separable. That is, they are described by an equation that does not allow one to factor the modes and polarizations separately. It is a type of superposition that gives rise to modes with space-variant polarization. The range of distinct modes that can be produced can be mapped onto geometrical representations [39], allowing an investigation of the variety of modes that can be produced and their underlying mathematical structure.

1.4.3 Poincaré Beams

When we do a superposition of spatial modes of different order and polarization, we get a mode where both orientation and ellipticity vary from point to point. To describe this in the simplest terms let us start with the Laguerre-Gauss and circular polarization bases, similar to Eq. 1.110 but now with the modes LG_0^ℓ and LG_0^0. This yields

$$U = \frac{1}{\sqrt{2}}(LG_0^\ell \hat{e}_R + LG_0^0 e^{-i\gamma}\hat{e}_L), \qquad (1.114)$$

The amplitude and phase of the two spatial modes do not have the same values at each point, and so they will yield in general elliptical states at any given point. If we use the expressions for each mode, we can rewrite Eq. 1.114 as

$$U = \frac{1}{\sqrt{2}}AGW\left(\cos\chi\,\hat{e}_R + \sin\chi\,e^{-i\gamma}\hat{e}_L\right), \qquad (1.115)$$

where now

$$\chi = \tan^{-1}\left(\frac{A_0}{A_\ell r^\ell}\right) \qquad (1.116)$$

and

$$\theta = \ell\phi/2 + \gamma/2, \qquad (1.117)$$

A is a constant and G and W are defined by Eqs. 1.68 and 1.69. Notice that the relative amplitude of the two states of polarization depends only on the radial coordinate, and the relative phase depends only on the angular coordinate. Let us consider the case $\ell = +1$. Since at $r = 0$ the amplitude of LG_0^{+1} is 0, while that of LG_0^0 is maximum, then at $r = 0$ the state of polarization is left circular. As r increases, the amplitude of LG_0^{+1} increases while the amplitude of LG_0^0 decreases, and at a certain radius r_v they will be

Complex Light Beams

equal and the polarization is linear. In the range $0 < r < r_v$ the polarization will be left-handed elliptical, with ellipticity that depends on r. For $r > r_v$ the amplitude of LG_0^{+1} will be greater than that of LG_0^0, and so the state of polarization will be right-handed, and at $r \to \infty$ the polarization will be right circular. The mode LG_0^{+1} has a phase that varies with ϕ whereas LG_0^0 has a constant phase. Therefore, the relative phase at a point (r, ϕ) is $\phi + \gamma$, and therefore the orientation of the elliptic-linear states is $\theta = \phi/2 + \gamma/2$. In all, this new mode has an ellipticity that varies with radial distance and an orientation that varies with ϕ. It contains a mapping of all the states on the Poincaré sphere onto the transverse beam mode, and for that they are called Poincaré beams. It yields the pattern of Fig. 1.22.(a). If we use $\ell = -1$ mode, we get the pattern of Fig. 1.22.(b). These two patterns are known as the lemon and the star; names derived from an analysis of their topological structure: line singularities [11, 19, 25], such as those found in fingerprints[43].

We can make two types of changes to Eq. 1.114 and get yet other polarization patterns. If we change the mode to $\ell = 2$, we get a radial mode but with an ellipticity that varies with r (see that Eq. 1.117 yields $\theta = \phi$ as in the radial vector mode). Conversely, we can change the set of states of polarization used to get an asymmetric polarization pattern, as shown in Fig. 1.22.(c) for the case of the linear x and y linear polarization states. This pattern is also of interest because it has a polarization gradient across its profile.
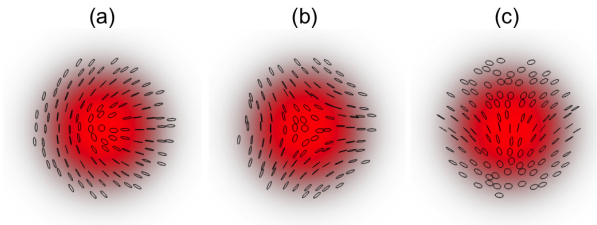

Figure 1.22.   Lemon (a) and star (b) Poincaré modes obtained using Laguerre Gauss modes respectvely with $\ell = 1$ and $\ell = -1$ in a state of right-hand circular polarization in superposition with fundamental mode in a state of left-hand circular polarization. (c) Same construction as for (a) but using states of linear polarization instead of circular states.

These types of modes can be produced with various laboratory designs that use superposition of collinear modes [27], or transmission through optical elements with dislocations, such as the q-plates [15], solids with stress birefringence [8] or optical fibers [31].

1.5 Discussion and Conclusions

The control of amplitude, phase and polarization of light has yielded an interesting set of optical beams presented in this chapter. They carry an array of unique properties, such as optical vortices, angular momentum, self reconstruction and vectorial dislocations, to name a few. They have already been at the center of many applications, and hold promise of more. Although these works have approached these beams from a classical perspective, their properties and applications extend to the quantum-physical domain, where they also provide settings for fundamental tests and applications. The field of complex light is growing into a one that provides an array of optical tools for research and applications. The present chapter presents an overview of what has been done, with the promise that more is yet to come.

36 | Complex Light Beams

Bibliography

[1] Allen, L., Barnett, S. M. and Padgett, M. J. (2003). Optical Angular Momentum (Institute of Physics, Bristol).

[2] Allen, L., Beijersbergen, M. W., Spreeuw, R. J. C. and Woerdman, J. P. (1992). Orbital angular momentum of light and the transformation of Laguerre-Gaussian laser modes, Phys. Rev. A 45, pp. 8185–8189.

[3] Arlt, J. and Dholakia, K. (2000). Generation of high-order Bessel beams by use of an axicon, Optics Commun 177, pp. 297–301.

[4] Ashkin, A. (1970). Acceleration and trapping of particles by radiation pressure, Phys. Rev. Lett. 24, pp. 156–159.

[5] Bandres, M. A. and Gutierrez-Vega, J. C. (2004). Ince-Gaussian beams, Opt. Lett. 29, pp. 144–146.

[6] Baumann, S. M., Kalb, D. M., MacMillan, L. H. and Galvez, E. J. (2009). Propagation dynamics of optical vortices due to Gouy phase, Opt. Express 17, pp. 9818–9827.

[7] Bazhenov, V. Y., Soskin, M. S. and Vasnetsov, M. V. (1992). Screw dislocations in light wavefronts, J. Mod. Opt. 39, pp. 985–990.

[8] Beckley, A. M., Brown, T. G. and Alonso, M. A. (2012). Full Poincaré beams II: partial polarization, Opt. Express 20, pp. 9357–9362.

[9] Beijersbergen, M. W., Allen, L., van der Veen, H. E. L. O. and Woerdman, J. P. (1993). Astigmatic laser mode converters and transfer of orbital angular momentum, Optics. Commun. 96, pp. 123–132.

[10] Berry, M. V. and Balazs, N. L. (1979). Nonspreading wave packets, Am. J. Phys. 47, pp. 264–267.

[11] Berry, M. V. and Hannay, J. H. (1977). Umbilic points on Gaussian random surfaces, J. Phys. A 10, pp. 1809–1821.

[12] Born, M. and Wolf, E. (1999). Principles of Optics (Cambridge).

[13] Bowman, R., D'Ambrosio, V., Rubino, E., Jedrkiewicz, O., Trapani, P. D. and Padgett, M. J. (2011). Optimisation of a low cost SLM for diffraction efficiency and ghost order suppression, Eur. Phys. J. 199, pp. 149–158.

[14] Broky, J., Siviloglou, G. A., Dogariu, A. and Christodoulides, D. N. (2008). Self-healing properties of optical Airy beams, Opt. Express

16, pp. 12880–12891.

[15] Cardano, F., Karimi, E., Marrucci, L., Lisio, C. and Santamato, E. (2013). Generation and dynamics of optical beams with polarization singularities, Opt. Express 21, pp. 8815–8820.

[16] Chavez-Cerda, S., Padgett, M. J., Allison, I., New, G. H. C., Gutierrez-Vega, J. C., O'Neil, A. T., Vicar, I. M. and Courtial, J. (2002). Holographic generation and orbital angular momentum of high-order Mathieu beams, J. Opt. B 4, pp. S52–S57.

[17] Collett, E. (1993). Polarized light: fundamentals and applications (Taylor and Francis).

[18] Davis, J. A., Carcole, E. and Cottrell, D. M. (1996). Nondiffracting interference patterns generated with programmable spatial light modulators, Appl. Opt. 35, pp. 599–602.

[19] Dennis, M. R. (2002). Polarization singularities in paraxial vector fields: morphology and statistics, Opt. Commun. 213, pp. 201–221.

[20] Dorn, R., Quabis, S. and Leuchs, G. (2003). Sharper focus for a radially polarized light beam, Phys. Rev. Lett. 91, pp. 233901–1–4.

[21] Durnin, J. (1987). Exact solutions for nondiffracting beams. I. the scalar theory, J. Opt. Soc. Am. A 4, pp. 651–654.

[22] Durnin, J., Miceli Jr., J. J. and Eberly, J. H. (1987). Diffraction-free beams, Phys. Rev. Lett. 58, pp. 1499–1501.

[23] Fahrbach, F. O. and Rohrbach, A. (2012). Propagation stability of self-reconstructing Bessel beams enables contrast-enhanced imaging in thick media, Nat. Commun. 3:632, pp. 1–8.

[24] Fontana, J. R. and Pantell, R. H. (1983). A high-energy,laser accelerator for using the inverse Cherenkov effect, J. Appl. Phys. 54, pp. 4285–4288.

[25] Freund, I. (2001). Polarization flowers, Opt. Commun. 199, pp. 47–63.

[26] Galvez, E. J. (2013). Vector beams in free space (Cambridge University Press, Cambridge), pp. 51–69.

[27] Galvez, E. J., Khadka, S., Schubert, W. H. and Nomoto, S. (2012). Poincaré-beam patterns produced by non-separable superpositions of Laguerre-Gauss and polarization modes of light, Appl. Opt. 51, pp. 2925–2934.

[28] Harke, B., Keller, J., Ullal, C. K., Westphal, V., Schonle, A. and Hell, S. W. (2008). Resolution scaleng in sted microscopy, Opt. Express 16, pp. 4154–4162.

[29] He, H., Friese, M. E. J., Heckenberg, N. R. and Rubinsztein-Dunlop, H. (1995). Direct observation of transfer of angular momentum to absorptive particles from a laser beam with a phase singularity, Phys. Rev. Lett. 75, pp. 826–829.

[30] Heckenberg, N. R., McDuff, R., Smith, C. P. and White, A. G. (1992). Generation of optical phase singularities by computer-

generated holograms, Opt. Lett. 17, pp. 221–223.

[31] Jayasurya, Y. V., Inavalli, V. V. G. K. and Viswanathan, N. K. (2011). Polarization singularities in the two-mode optical fiber output, Appl. Opt. 50, pp. 131–137.

[32] Jones, P. H., Marago, O. M. and Volpe, G. (2015). Optical Tweezers Principles and Applications (Cambridge University Press, Cambridge).

[33] Lang, M. J. and Block, S. M. (2003). Resource letter: Lbot-1: Laser-based optical tweezers, Am. J. Phys. 71, pp. 201–215.

[34] Leach, J., Wulff, K., Sinclair, G., Jordan, P., Courtial, J., Thompson, L., Gibson, G., Karundi, K., Cooper, J., Laczik, Z. J. and Padgett, M. (2006). Interactive approach to optical tweezers control, Appl. Opt. 45, pp. 897–903.

[35] Lin, Y., Seka, W., Eberly, J., Huang, H. and Brown, D. (1992). Experimental investigation of bessel beam characteristics, Appl. Opt. 31, pp. 2708–2713.

[36] Mair, A., Vaziri, A., Weihs, G. and Zeilinger, A. (2001). Entanglement of the orbital angular momentum states of photons, Nature 412, pp. 313–316.

[37] Marrucci, L., Manzo, C. and Paparo, D. (2006). Optical spin-to-orbital angular momentum conversion in inhomogeneous anisotropic media, Phys. Rev. Lett. 96, pp. 163905 1–4.

[38] McGloin, D. and Dholakia, K. (2005). Bessel beams: diffraction in a new light, Contemp. Phys. 46, pp. 15–28.

[39] Milione, G., Sztul, H. I., Nolan, D. A. and Alfano, R. R. (2011). Higher-order Poincaré sphere, stokes parameters, and the angular momentum of light, Phys. Rev. Lett. 107, pp. 053601 1–4.

[40] Milonni, P. W. and Eberly, J. H. (1988). Lasers (John Wiley & Sons, New York).

[41] Padgett, M. J., Molloy, J. and McGloin, D. (2010). Optical Tweezers: Methods and Applications (CRC Press Taylor and Francis Group, Boca Raton).

[42] Pedrotti, F. L. and Pedrotti, L. S. (1993). Introduction to Optics (Prentice Hall).

[43] Penrose, R. (1979). The topology of ridge systems, Ann. Hum. Genet., Lond. 42, pp. 435–444.

[44] Planchon, T. A., Gao, L., Milkie, D. E., Galbraith, J. A., Galbraith, C. G. and Betzig, E. (2011). Rapid three-dimensional isotropic imaging of living cells using bessel beam plane illumination, Nat. Meth. 8, pp. 417–423.

[45] Siegman, A. E. (1986). Lasers (University Science Books, Mill Valley).

[46] Siviloglou, G. A., Broky, J., Dogariu, A. and Christodoulides, D. N. (2008). Ballistic dynamics of Airy beams, Opt. Lett. 33, pp. 207–

209.

[47] Smith, S. P., Bhalotra, S. R., Brody, A. L., Brown, B. L., Boyda, E. K. and Prentiss, M. (1999). Inexpensive optical tweezers for undergraduate laboratories, Am. J. Phys. 67, pp. 26–35.

[48] Sztul, H. I. and Alfano, R. R. (2008). The Poynting vector and angular momentum of Airy beams, Opt. Express 16, pp. 9411–9416.

[49] Tlusty, T., Meller, A. and Bar-Ziv, R. (1998). Optical gradient forces in strongly localized fields, Phys. Rev. Lett. 81, pp. 1738–1741.

[50] Torok, P. and Munro, P. R. T. (2004). The use of Gauss-Laguerre vector beams in STED microscopy, Opt. Express 12, p. 3605.

[51] Turunen, J., Vasara, A. and Friberg, A. T. (1988). Holographic generation of diffraction-free beams, Appl. Opt. 27, pp. 3959–3962.

[52] Vasara, A., Turunen, J. and Friberg, A. T. (1989). Realization of general non diffracting beams with computer-generated holograms, J. Opt. Soc. Am. A 6, pp. 1748–1754.

[53] Vasilyeu, R., Dudley, A., Khilo, N. and Forbes, A. (2009). Generating superpositions of higher-order Beasel beams, Opt. Express 17, pp. 23389–23395.

[54] Vettenburg, T., Dalgarno, H. I. C., Nylk, J., Llado, C. C., Ferrier, D. E. K., Cizmar, T., Gunn-Moore, F. J. and Dholakia, K. (2014). Light sheet microscopy using an Airy beam, Nat. Meth. 11, pp. 541–544.

[55] Zhan, Q. (2009). Cylindrical vector beams: from mathematical concepts to applications, Adv. Opt. Photonics 1, pp. 1–57.